MIT Libraries | DSpace@MIT

MIT Open Access Articles

SPATIALLY RESOLVED STAR FORMATION IMAGE AND THE ULTRALUMINOUS X-RAY SOURCE POPULATION IN NGC 2207/IC 2163

Massachusetts Institute of Technology

SPATIALLY RESOLVED STAR FORMATION IMAGE AND THE ULTRALUMINOUS X-RAY SOURCE POPULATION IN NGC 2207/IC 2163

S. MINEO[1], S. RAPPAPORT[2,3], B. STEINHORN[4], A. LEVINE[5], M. GILFANOV[6,7], AND D. POOLEY[3]

[1] Harvard-Smithsonian Center for Astrophysics, 60 Garden Street Cambridge, MA 02138, USA; smineo@head.cfa.harvard.edu
[2] 37-602B, M.I.T. Department of Physics and Kavli Institute for Astrophysics and Space Research, 70 Vassar Street, Cambridge, MA 02139, USA; sar@mit.edu
[3] Eureka Scientific, 5248 Valley View Road, El Sobrante, CA 94803-3435, USA; pooley@gmail.com
[4] Harvard-MIT Division of Health Sciences and Technology, Harvard Medical School, 260 Longwood Avenue, Boston, MA 02115, USA; bsteinho@mit.edu
[5] M.I.T. Kavli Institute for Astrophysics and Space Research, Room 37-575, 70 Vassar Street, Cambridge, MA 02139, USA; aml@space.mit.edu
[6] Max Planck Institut für Astrophysik, Karl-Schwarzschild-Str. 1, D-85741 Garching, Germany; gilfanov@mpa-garching.mpg.de
[7] Space Research Institute of Russian Academy of Sciences, Profsoyuznaya 84/32 117997 Moscow, Russia

ABSTRACT

The colliding galaxy pair NGC 2207/IC 2163, at a distance of ~39 Mpc, was observed with *Chandra*, and an analysis reveals 28 well resolved X-ray sources, including 21 ultraluminous X-ray sources (ULXs) with $L_X \gtrsim 10^{39}$ erg s^{-1}, as well as the nucleus of NGC 2207. The number of ULXs is comparable with the largest numbers of ULXs per unit mass in any galaxy yet reported. In this paper we report on these sources, and quantify how their locations correlate with the local star formation rates seen in spatially resolved star formation rate density images that we have constructed using combinations of *GALEX* FUV and *Spitzer* 24 μm images. We show that the *numbers* of ULXs are strongly correlated with the local star formation rate densities surrounding the sources, but that the *luminosities* of these sources are not strongly correlated with star formation rate density.

Key words: binaries: general – galaxies: individual (NGC 2207/IC 2163) – galaxies: interactions – galaxies: nuclei – galaxies: starburst – galaxies: structure – stars: formation – stars: luminosity function, mass function – stars: neutron

Online-only material: color figures

1. INTRODUCTION

Galaxy collisions can provide information on (1) galaxy dynamics, (2) triggers of star formation, and (3) the origins of ultraluminous X-ray sources, i.e., off-nuclear X-ray point sources whose luminosity exceeds the maximum isotropic emission expected from a ~10 $M_\odot$ black hole (BH): $L_X \gtrsim 10^{39}$ erg s^{-1} (hereafter, "ULXs;" see review by Feng & Soria 2011). When one or both of the colliding galaxies have a high gas content, spectacular bursts of star formation may be triggered. Some fraction of the more massive stars ($\gtrsim 10 M_\odot$) that happen to be formed in binary systems evolve to become high-mass X-ray binaries (HMXBs) with neutron-star (NS) or stellar-mass BH accretors. Substantial numbers of ULXs may also be produced. The Antennae (Whitmore & Schweizer 1995; Zezas & Fabbiano 2002), the Cartwheel (Higdon 1995; Gao et al. 2003; Wolter et al. 2006), and Arp 147 (Rappaport et al. 2010) grandly illustrate these phenomena. Although the accepted assumption was that HMXBs would be Eddington limited ($L_X \lesssim 10^{39}$ erg s^{-1}), there is a growing body of evidence linking ULXs to these sources (e.g., Grimm et al. 2003; Fabbiano 2005; Mineo et al. 2012).

Compelling simulations of colliding galaxies have been carried out (see, e.g., Lynds & Toomre 1976; Toomre 1978; Gerber et al. 1992; Mihos & Hernquist 1994; Appleton et al. 1996; Higdon & Wallin 1997; Struck et al. 2005), and have produced examples that are remarkably similar in appearance to the most tidally disturbed collisional pairs.

The ULXs seen in these galaxies are of special interest, especially those with $L_X \gtrsim 10^{40}$ erg s^{-1}. Assuming that these objects are BHs accreting at the Eddington limit, their luminosity gives a limit on the mass of the accreting BH of ~50–100 $M_\odot$. These masses are substantially higher than those

of Galactic BHs ($M \lesssim 20 M_\odot$; Özel et al. 2010) and could be related to the metallicity of the host galaxy (e.g., Belczynski et al. 2010; Mapelli et al. 2010). The population of ULXs may therefore consist of sources of a different nature, depending on their luminosity. Sources with $L_X \lesssim 10^{40}$ erg s^{-1} might be powered by accreting BHs of mass $3 M_\odot \lesssim M \lesssim 100 M_\odot$, whereas the nature of the brightest sources ($L_X \gtrsim 10^{40}$ erg s^{-1}) still represents an enigma. They might be ~10–20 $M_\odot$ BHs emitting at ~5 times the Eddington luminosity, BHs with masses ~100 $M_\odot$ emitting at the Eddington limit, or the so-called intermediate-mass black holes ("IMBHs," $10^2 M_\odot \lesssim M \lesssim 10^5 M_\odot$; see, e.g., Colbert & Mushotzky 1999) emitting below the Eddington limit, or some combination thereof. At the highest end of the ULX luminosity function (approaching ~10^{41} erg s^{-1}) it becomes increasingly difficult to see how the requisite luminosity, even if somewhat beamed, could be radiated near a stellar-mass BH (see, e.g., Madhusudhan et al. 2008). The maximum observed luminosity for such sources is ~10^{42} erg s^{-1} (Farrell et al. 2009).

The IMBHs are of extreme importance as they are thought to be the building blocks of super-massive BHs ("SMBHs" $M \sim 10^6 M_\odot$; e.g., Volonteri 2010). However, a conceptual problem with IMBH accretors is their formation and their subsequent capture of a massive donor star. Portegies Zwart et al. (2004), among others, have proposed that runaway star collisions in newly formed massive star clusters lead to the formation of supermassive stars (e.g., $\gtrsim 500 M_\odot$) which, in turn, evolve to form IMBHs. Theoretical problems with this scenario include the highly uncertain evolution of supermassive stars, and an implausibly high efficiency for producing the requisite numbers of IMBHs (see King 2004).

Previous studies have shown a correlation between the *overall* star formation rate (hereafter "SFR") in a galaxy and
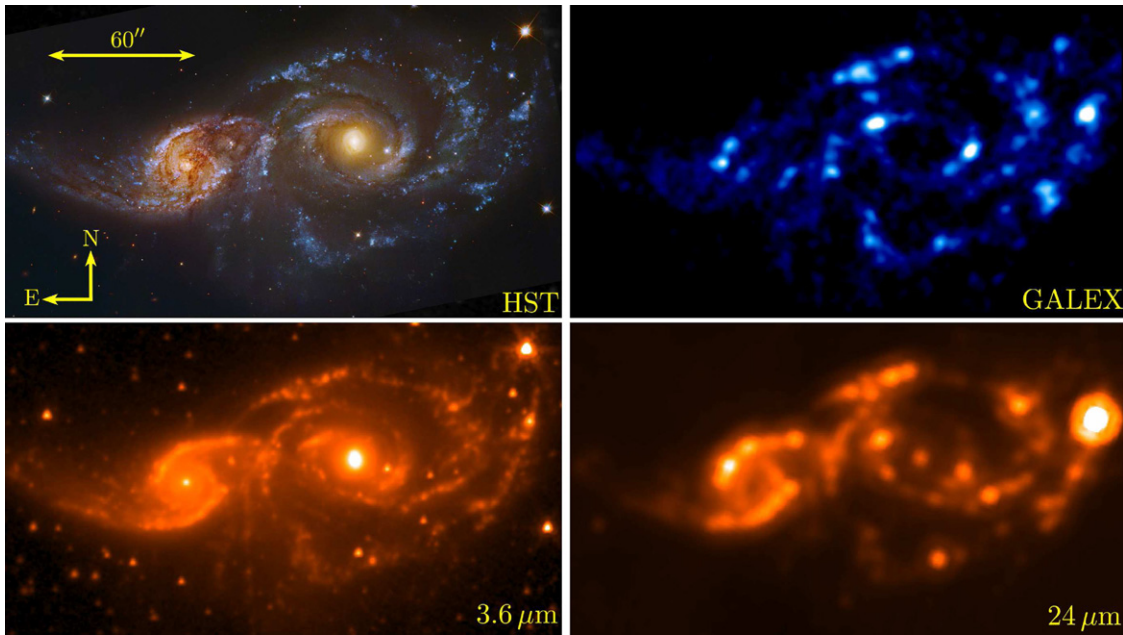
Figure 1. Montage of images of NGC 2207/IC 2163 taken with *HST*, *GALEX* (FUV), and *Spitzer* (3.6 and 24 μm). The distance to these galaxies is $\sim$39 Mpc.
(A color version of this figure is available in the online journal.)

the number of luminous X-ray sources (e.g., Grimm et al. 2003; Mapelli et al. 2010; Swartz et al. 2011; Mineo et al. 2012; Smith et al. 2012). The SFRs may be estimated using any of a wide variety of indicators: ultraviolet (UV) continuum, recombination lines (Hα), forbidden lines ([O II]), far-infrared (FIR) continuum, thermal radio emission luminosities individually, or in combination (see, e.g., Kennicutt 1998, for a review). Leroy et al. (2008) suggest that a linear combination of the *GALEX* FUV and *Spitzer* 24 μm bands (see their Equations (D10) and (D11)) is particularly good in this respect. It is possible to follow Leroy et al. and utilize this prescription to produce complete SFR images of galaxies with a few arcsec resolution.

In this paper we introduce a new technique to investigate the relation between the number and luminosity of bright X-ray point sources and the *local* surrounding SFR. This allows us to probe these relations even in the case of small numbers of luminous X-ray sources. The analysis involves a direct quantitative comparison of the spatial structures in these SFR images with the *Chandra* X-ray images. In addition, as has been discussed (Calzetti et al. 2007; S. Rappaport et al. 2012, in preparation; M. Krumholz 2012, private communication), the *GALEX* intensities tend to indicate the somewhat older regions of star formation ($\gtrsim$30 Myr, after the obscuring dust has already been cleared), while the *Spitzer* 24 μm images reveal younger star formation (i.e., 5–10 Myr, and still dust enshrouded) which may be more closely related to the upper end of the ULX luminosities (i.e., with $L_X \gtrsim 10^{40}$ erg s^{-1}). (See also the closely related work of Swartz et al. 2009; Yukita et al. 2010; Kaufman et al. 2012.) Thus, some of the theoretical ideas concerning the formation and evolution of very massive binaries can be investigated.

We report here on our analysis of the relation between the location of luminous X-ray sources and the SFR density in the colliding galaxy pair NGC 2207 and IC 2163 (see, e.g., Kaufman et al. 2012). We utilize archival *Chandra*, *GALEX*, *Spitzer* and Two Micron All Sky Survey (2MASS) images of these galaxies. The galaxy pair is at an estimated distance of

$39.6^{+5.9}_{-5.1}$ Mpc (Arnett 1982). This is the redshift-independent distance with the smallest uncertainty provided by the NASA/IPAC Extragalactic Database (NED),[8] and it is based on SN Ia measurements. A montage of images of NGC 2207/IC 2163 taken with *Hubble Space Telescope* (*HST*), *GALEX*, and *Spitzer* is shown in Figure 1 (NGC 2207 is the larger galaxy on the right). Our analysis of the archival *Chandra* data reveal a total of 22 X-ray point sources with $L_X \gtrsim 10^{39}$ erg s^{-1} within the $D25$ ellipse of NGC 2207 & IC 2163 (de Vaucouleurs et al. 1991). Such a production efficiency of luminous X-ray sources per unit stellar mass is comparable with that of the Antennae pair of colliding galaxies (see Section 4.2 and Table 2).

Another advantage of studying the colliding galaxy pair NGC 2207/IC 2163, in addition to the fact that it is relatively close and well studied in numerous wavebands, is that the dynamics of its collision have been extensively modeled (see, e.g., Struck et al. 2005 and references therein). Struck et al. (2005) find that their most successful model, which best reproduces the current geometry and morphology of the two galaxies, has the following starting conditions. The two galaxies are very roughly coplanar as is the grazing collision trajectory between them. The disk planes of these galaxies are inclined by only a modest amount (e.g., $\sim$25°–50°) with respect to the plane of the sky. The best model results are obtained if the two galaxies had their closest approach during their first pass when IC 2163 was on the western side of NGC 2207 (see Figure 1) some 300 Myr in the past. The orbit of the two galaxies is counterclockwise in Figure 1 as is the intrinsic rotation of IC 2163, i.e., the collision is prograde with respect to the more compact galaxy. By contrast, the more expansive galaxy, NGC 2207, is rotating the opposite way, and the collision is retrograde with respect to it. The simulations show that the spiral arms of NGC 2207 were present before the collision, and are not much perturbed by the collision whereas the prominent "ocular" feature in IC 2163 (see especially the *Spitzer* images) was created by the encounter, and its existence apparently shows that the collision cannot have

---

[8] http://ned.ipac.caltech.edu/

been going on for more than an orbit of the two galaxies. Any star formation that the grazing collision has induced has likely been ongoing for the past few hundred Myr. The total masses (including the dark-matter halos) of the two galaxies were taken to be 1.5×10^{11} and 1.1×10^{11} $M_\odot$ for NGC 2207 and IC 2163, respectively.

2. X-RAY ANALYSIS

2.1. Data Preparation

We analyzed the publicly available *Chandra* ACIS-S observation of the galaxy pair NGC 2207–IC 2163, having identification number 11228 and an exposure time of 13 ks. The data preparation was done following the standard CIAO[9] threads (CIAO version 4.3, CALDB version 4.5.1) for soft (0.5–2 keV), hard (2–8 keV), and broad (0.5–8.0 keV) energy bands. The point source detection was performed in the broad band using CIAO `wavdetect`, over the area within the $D25$ ellipse of NGC 2207 and IC 2163. We used the $\sqrt{2}$ series from 1.0 to 8.0 as the scale parameter, in order to account for the variation of the effective width of the *Chandra* point spread function (PSF) from the inner to the outer parts of the analyzed observation, with reference to the *Chandra* aim point. We set the value of the parameter `sighthresh` as the inverse of the total number of pixels in the image ($\sim 10^{-6}$), in order to have one spurious detection per field. We used `maxiter = 10`, `iterstop = 0.00001` and `bkgsigthresh = 0.0001`. The encircled fraction of source energy used for source estimation (parameter `eenergy`) was set to 0.8.

We computed a monochromatic exposure map for the mean photon energy, i.e., 1.25 keV (soft band), 5.0 keV (hard band), and 4.25 keV (broad band), of each band. This was done using the CIAO script `fluximage`, which runs the tool `mkinstmap` to calculate the instrument map, i.e., the effective-area-weighted exposure map in instrument coordinates, for the center of each energy band, and `mkexpmap` to calculate the exposure maps in sky coordinates for each energy band. The exposure maps allow us to measure fluxes and hardness ratios for the detected X-ray point-like sources, using the photometric procedure described below.

2.2. Source Counts

For each detected point source we measured the count rate inside a circular region centered at the source central coordinates produced by `wavdetect`. The size of the circular region for individual sources was determined by requiring the encircled PSF energy to be 85% of the total PSF energy. In order to do so, the PSF at the position of each point source was first constructed and then mapped into the World Coordinate System (WCS) reference frame of the relative point source image using the CIAO tasks `mkpsf` and `reproject_image`, respectively. The background regions were defined as annuli having an inner radius equal to the radius of the source region and an outer radius that is three times larger. The corrected source counts and errors were obtained by performing aperture-corrected photometry, following the same method as in Voss & Gilfanov (2007) and Mineo et al. (2012):

$$S = \frac{(b-d)C - dQ}{b\alpha - d\beta} \qquad (1)$$

---

9 http://cxc.harvard.edu/ciao4.3/index.html

$$\sigma_S^2 = \frac{(b-d)^2 \sigma_C^2 + d^2 \sigma_Q^2}{(b\alpha - d\beta)^2}. \qquad (2)$$

Here, S is the number of net counts from the source, C is the number of counts inside the source region and Q is the number of counts in the background region, α is the integral of the PSF over the source region (expressed as a fraction of the total PSF energy), β is the corresponding integral of the PSF over the source and background regions, b is the integral of the (effective-area weighted) exposure over the source and background regions, and d is the exposure integrated over the source region.

We found four compact sources having background regions that overlap their neighboring sources. In these cases the source count estimation is compromised and it was corrected as follows. For the overlapping point sources we defined the radius of the circular region that included 90% of the encircled PSF. We excluded these regions from both the image and exposure map in order to respectively subtract the source contribution from the background counts and correct the source area. Finally, we again performed the aperture-corrected photometry described above using the corrected image and exposure map.

2.3. Luminosities and Hardness Ratios

X-ray fluxes in the 0.5–8.0 keV band were estimated from the count rates measured for each source as described in the previous section. A counts-to-erg conversion factor was obtained by first extracting the *combined* spectrum of all point sources detected within the $D25$ ellipse, except the central source in NGC 2207, which may be an active galactic nucleus (AGN) partially covered by dense clouds (Elmegreen et al. 2006; Kaufman et al. 2012). A background spectrum was extracted from large regions located far from detected point sources but on the same CCD chip as the galaxy pair under study. Some of the background regions were located between point sources within the $D25$ ellipse in order to account for the diffuse emission contribution of the galaxy itself.

Source and background spectra were created using the CIAO task `dmextract` and the associated weighted ARF and RMF files were made using, respectively, the tasks `mkwarf` and `mkrmf`. The average source spectrum was binned so as to have a minimum of 20 total counts (i.e., not background subtracted) per channel and thereby facilitate minimum-χ^2 fitting. The background-subtracted spectrum was modeled as an absorbed power law using XSPEC v. 12.7.1b. The best-fit model was obtained for $n_H = 2.88^{+0.15}_{-0.13} \times 10^{21}$ cm^{-2} and photon power-law index $\Gamma = 2.08^{+0.34}_{-0.31}$ with $\chi^2 = 15.37$ for 21 degrees of freedom. The best-fit power-law index is consistent with the centroid of the power law photon index distribution for luminous X-ray compact sources in star-forming galaxies, $\Gamma = 1.97 \pm 0.11$ (Swartz et al. 2004). The best-fit column density is a factor of ~ 3 larger than the average Galactic n_H in this direction seen in the Leiden/Argentine/Bonn (LAB) Survey of Galactic H I (Kalberla et al. 2005).

The best-fit spectral model was used to convert the count rates of each of the detected point sources into fluxes (erg cm^{-2} s^{-1}). X-ray luminosities were calculated assuming the distance of 39.6 Mpc (Arnett 1982).

Hardness ratios were used to investigate the spectral properties of the sources detected in the 0.5–8 keV band. The procedure described in Section 2.2 was applied to the reference source list in both soft (S: 0.5–2 keV) and hard (H: 2–8 keV) bands. The respective source counts were used to calculate the X-ray hardness

Table 1
NGC 2207/IC 2163 X-Ray Source Properties

Source	α_{J2000} (deg)	δ_{J2000} (deg)	0.5–8 keV (cts)	Signif (σ)	0.5–2 keV (counts)	2–8 keV (counts)	HR (counts)	L_X (10^{38} erg s^{-1})	F_X (10^{-14} erg cm^{-2} s^{-1})
(1)	(2)	(3)	(4)	(5)	(6)	(7)	(8)	(9)	(10)
1	94.08436	−21.3851	20 ± 6.1	8	14 ± 5.4	5.9 ± 4	−0.41 ± 0.32	24 ± 7.3	1.26 ± 0.39
2	94.07186	−21.3806	40 ± 8.5	18	29 ± 7.5	11 ± 5.2	−0.46 ± 0.21	47 ± 10	2.51 ± 0.54
3	94.07053	−21.3758	18 ± 6.3	9.4	7 ± 4.6	11 ± 5.2	0.23 ± 0.38	22 ± 7.8	1.18 ± 0.41
4	94.06623	−21.3757	91 ± 12	40	61 ± 10	30 ± 7.5	−0.35 ± 0.13	110 ± 14	5.73 ± 0.76
5	94.07828	−21.3743	27 ± 7.4	12	18 ± 6.3	8.8 ± 4.9	−0.35 ± 0.29	32 ± 8.7	1.68 ± 0.46
6	94.06943	−21.3743	20 ± 6.1	9.5	18 ± 5.8	2.1 ± 3	−0.80 ± 0.27	25 ± 7.5	1.34 ± 0.40
7[a]	94.09183	−21.3727	76 ± 11	28	9.2 ± 5.2	66 ± 10	0.76 ± 0.12	90 ± 13	4.78 ± 0.69
8	94.07010	−21.3726	7.3 ± 4.4	3	3.7 ± 3.6	3.7 ± 3.6	0.00 ± 0.69	9.1 ± 5.4	0.48 ± 0.29
9	94.11187	−21.3697	14 ± 5.4	5.5	13 ± 5.3	1.2 ± 2.8	−0.83 ± 0.37	21 ± 7.9	1.10 ± 0.42
10	94.08552	−21.3696	27 ± 6.8	11	21 ± 6.1	6.7 ± 4.1	−0.51 ± 0.25	32 ± 8.1	1.72 ± 0.43
11	94.07498	−21.3679	33 ± 7.4	15	27 ± 6.8	6.6 ± 4.1	−0.60 ± 0.21	41 ± 9.1	2.19 ± 0.48
12	94.10386	−21.3641	7 ± 4.3	2.8	4.6 ± 3.8	2.4 ± 3.2	−0.32 ± 0.70	8.3 ± 5.1	0.44 ± 0.27
13	94.08058	−21.3642	14 ± 5.2	5.6	11 ± 4.9	2.3 ± 3	−0.67 ± 0.39	16 ± 6.1	0.86 ± 0.33
14	94.09434	−21.3608	26 ± 6.8	12	16 ± 5.7	9.5 ± 4.7	−0.27 ± 0.28	31 ± 8.1	1.64 ± 0.43
15	94.07195	−21.3599	16 ± 5.5	7.8	9.9 ± 4.6	6.5 ± 4	−0.20 ± 0.37	19 ± 6.6	1.03 ± 0.35
16	94.07056	−21.3527	29 ± 6.9	14	21 ± 6.1	7.5 ± 4.3	−0.48 ± 0.24	35 ± 8.3	1.84 ± 0.44
17	94.10830	−21.3771	15 ± 5.6	5.6	7.1 ± 4.3	8.1 ± 4.5	0.07 ± 0.41	21 ± 7.6	1.10 ± 0.40
18	94.10480	−21.3749	17 ± 6.1	6.2	9.3 ± 4.8	8.1 ± 4.6	−0.07 ± 0.39	21 ± 7.4	1.12 ± 0.39
19	94.07529	−21.3686	7.5 ± 4.3	3.4	6.5 ± 4.1	0.94 ± 2.6	−0.75 ± 0.63	9.2 ± 5.3	0.49 ± 0.28
20	94.07520	−21.3648	9.9 ± 5.3	8.5	4.1 ± 4.1	5.7 ± 4.4	0.16 ± 0.61	12 ± 6.5	0.65 ± 0.35
21	94.11826	−21.3609	17 ± 5.8	7.4	13 ± 5.2	4.6 ± 3.7	−0.47 ± 0.35	24 ± 8	1.28 ± 0.42
22	94.10091	−21.3865	8.3 ± 4.5	3.3	8.3 ± 4.5	0 ± 2.2	−1.00 ± 0.53	12 ± 6.6	0.65 ± 0.35
23	94.08575	−21.3719	8 ± 4.3	3	4.5 ± 3.6	3.4 ± 3.4	−0.14 ± 0.62	9.4 ± 5.1	0.50 ± 0.27
24	94.11424	−21.3712	6.2 ± 4.2	2.3	5 ± 4	1.2 ± 2.9	−0.60 ± 0.79	9 ± 6.1	0.48 ± 0.33
25	94.11039	−21.3701	11 ± 5.1	5	10 ± 5	1 ± 2.8	−0.81 ± 0.46	14 ± 6.5	0.76 ± 0.35
26	94.10103	−21.3627	10 ± 4.9	4.6	5.5 ± 4	4.5 ± 3.8	−0.10 ± 0.55	12 ± 5.8	0.63 ± 0.31
27	94.12492	−21.3790	30 ± 7.3	9.9	22 ± 6.5	7.2 ± 4.3	−0.51 ± 0.25	37 ± 9	1.95 ± 0.48
28[b]	94.06592	−21.3673	6.8 ± 4.8	5.8	7.3 ± 4.8	0 ± 2.3	−1.00 ± 0.64	8 ± 5.7	0.43 ± 0.30

Notes. Column 1: source number, Column 2: right ascension (R.A.); Column 3: declination (Decl.); Column 4: net counts in broad (0.5–8 keV) band, computed with Equations (1) and (2). The uncertainty expressed here takes into account the fluctuations in the source as well as in the background; Column 5: broad band source detection significance from `wavdetect`. This computes how unlikely it is for the background in the customized PSF region to fluctuate to yield the detected number of counts. Note that the PSF region is optimized differently in `wavdetect` than in the calculation of Column 4 and is typically larger than in the latter; Columns 6 and 7: net counts in soft (0.5–2 keV) and hard (2–8 keV) bands respectively, computed with Equation (1). Uncertainties in net counts are quoted to 1σ and were obtained by mean of Equation (2); Column 8: hardness ratio, computed with Equation (3). Uncertainties were obtained by applying error propagation to the uncertainties in the net counts; Column 9: X-ray luminosity in the 0.5–8 keV band; Column 10: X-ray flux in the 0.5–8 keV band.
[a] Central active galactic nucleus.
[b] Extended soft X-ray source.

ratio as

$$\mathrm{HR} = \frac{\mathrm{H} - \mathrm{S}}{\mathrm{H} + \mathrm{S}}. \qquad (3)$$

3. LUMINOUS X-RAY SOURCES

3.1. Discrete Source Content

Following the method of Voss & Gilfanov (2006), we computed the completeness function $K(L_X)$ of the present *Chandra* observations of the $D25$ region. At the assumed distance of 39.6 Mpc, the luminosity, for which >80% of point sources are detected in the 0.5–8 keV band, is $L_{comp} \simeq 1.0 \times 10^{39}$ erg s^{-1} (equivalently, $K(L_{comp}) = 0.8$).

The properties of the discrete luminous X-ray sources that our analysis yielded for NGC 2207/IC 2163 are summarized in Table 1. In particular, for all sources detected within the $D25$ ellipse, we list the source location, the net counts after background subtraction in several bands, the hardness ratio (defined above), the X-ray luminosity, and the X-ray flux. The source counts in the 0.5–8 keV band were computed from Equations (1) and (2), and their associated uncertainties

are listed in Column 4. These values are used to compute the corresponding source fluxes and luminosities, as well as their uncertainties (Columns 10 and 9). By contrast, the detection significances listed in Column 5 were calculated by `wavdetect`. Most of the detection significances have a sensible correspondence with the source-count uncertainties listed in Column 4; however, the former expresses the probability that the background could fluctuate to yield the number of observed counts, whereas the latter also includes the fluctuations in the source counts themselves (for brighter sources this is actually the dominant contribution). The two columns are in reasonable accord given the different questions that they address. A possible exception is source No. 28. According to the `wavdetect` output, the net source counts for this object in the 0.5–8 keV band are 13.9 ± 3.9, while the detection significance is 5.8σ. This is attributed to the fact that source region defined by `wavdetect` is larger (by nearly a factor of two) than what we used to derive the results in Column 4 from Equations (1) and (2). We note, however, that we use the `wavdetect` output only to ascertain the existence of a source and to determine the source coordinates. By contrast,
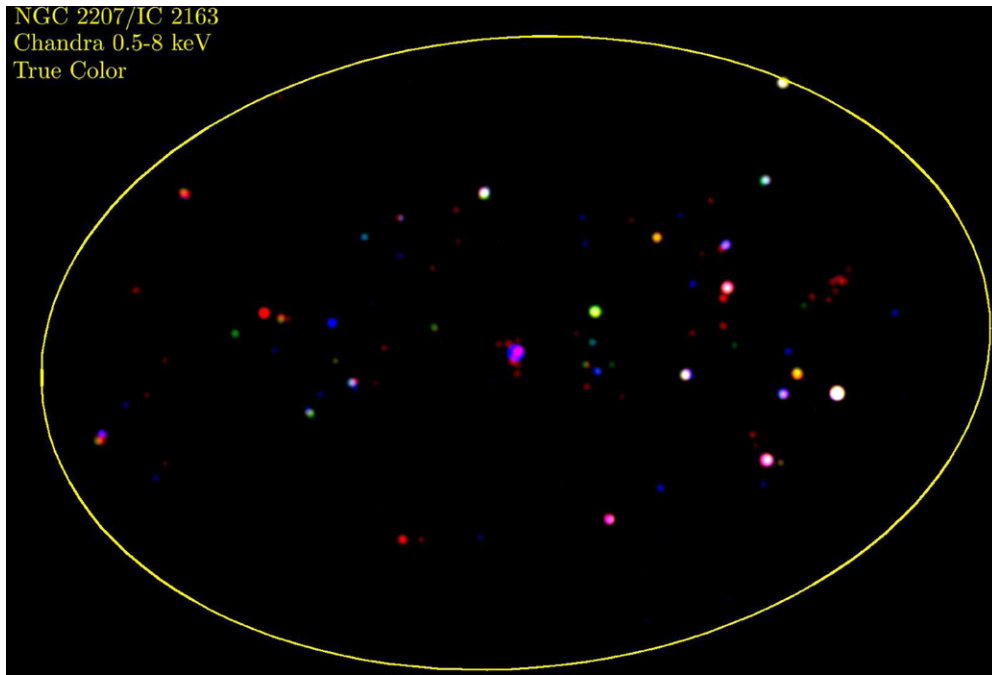
Figure 2. *Chandra* X-ray image, smoothed with a Gaussian kernel of $\sigma = 2\farcs5$ of the galaxy pair NGC 2207/IC 2163. The red color corresponds to the soft (0.2–1.5 keV) band, the green color to the medium (1.5–2.5 keV) band, and the blue color to the hard (2.5–8.0 keV) band. Note that the definition of "soft" and "hard" in the production this figure is different than that used in the data analysis and calculation of hardness ratio. The $D25$ ellipse is superposed for reference.

(A color version of this figure is available in the online journal.)

we perform X-ray photometry, as described in Section 2.2, utilizing somewhat different source regions than those defined by `wavdetect`; therefore, the detection significances in Column 5 do not exactly correspond to the net source counts listed in Column 4. We select the source sample to be analyzed by means of the incompleteness analysis, which accounts for the sensitivity variations across the image. The *Chandra* X-ray image is shown in Figure 2.

In all, 28 sources were detected, one of which (source No. 7) is likely a low-luminosity AGN associated with NGC 2207 (Kaufman et al. 2012), and 6 are just below our completeness threshold (as well as below the "ULX limit" of 10^{39} erg s^{-1}; see Section 3.2). A total of 21 sources are sufficiently bright to be ULXs. We note that source No. 28 has a soft spectrum, and may be part of an elongated soft X-ray feature. It is located in the outer spiral arm of NGC 2207, $\sim 1\farcm5$ N–W from its center at the location of the dusty starburst region called *feature i* (Elmegreen et al. 2000).

In order to show the distribution of the ULX population with respect to the morphological structures of the galaxy pair, we plot the X-ray point sources detected above the completeness limit, superposed on the *HST* image of NGC 2207/IC 2163 in Figure 3. The red circles indicate the location of individual ULXs, the circle size being proportional to the cube root of the 0.5–8 keV luminosity of the given X-ray source.

3.2. X-Ray Luminosity Function

Twenty-one compact sources with luminosities above L_{comp} were detected within the $D25$ region. Their luminosities range from 1.2×10^{39} erg s^{-1} to 1.1×10^{40} erg s^{-1}. We constructed the cumulative X-ray luminosity function (XLF), and it is shown in Figure 4. We modeled the XLF with a single-slope power law with a high luminosity cut-off exceeding the luminosity of the brightest compact source detected in the galaxy pair:

$$\frac{dN}{dL_{38}} = \xi \times L_{38}^{-\gamma}, \; L \leqslant 10^{41} \text{ erg s}^{-1}. \tag{4}$$

A fit of the cumulative XLF using a maximum likelihood method yielded a slope of $\gamma = 2.35^{+0.33}_{-0.29}$. We performed a Kolmogorov–Smirnov (KS) test to determine the goodness of fit. The D value obtained for the KS test is 0.24 for 21 sources corresponding to a significance level of $\sim 15\%$ that the data and model are from different distributions. This indicates that the model describes the data fairly well.

This slope is steeper than the slope of ~ 1.6 that is typically found for HMXB luminosity distributions below $\sim 10^{40}$ erg s^{-1} (Grimm et al. 2003; Swartz et al. 2011; Mineo et al. 2012). On the other hand, due to the limited sensitivity of this *Chandra* observation we may be sampling only the roll-off of the power-law distribution that extends beyond the abovementioned slope at lower luminosities to values of L_X in the range of ~ 1–3×10^{39} erg s^{-1}. A similar XLF slope, of $\gamma = 2.62^{+0.64}_{-0.50}$, is observed in one of the star-forming galaxies in the sample of Mineo et al. (2012), NGC 3079, for compact sources detected above a completeness limit of $\sim 10^{38}$ erg s^{-1}.

Interestingly, there is a lack of sources brighter than $\sim 10^{40}$ erg s^{-1} in NGC 2207/IC 2163. On the other hand, assuming the HMXB luminosity function from Mineo et al. (2012), and rescaling it to match the observed number of sources in NGC 2207/IC 2163, the predicted number of HMXBs above 10^{40} erg s^{-1} is 2.4 ± 1.5 (assuming a Poisson distribution), which is fairly consistent with what we observe. W. Luangtip et al. (in preparation) found the same evidence of a lack of sources brighter than $\sim 10^{40}$ erg s^{-1} in a sample of 17 luminous infrared galaxies located at distances between ~ 14 and ~ 61 Mpc. This may be due to the fact that the brightest ULXs should have very short lifetimes (e.g., $\lesssim$few $\times 10^6$ yr; see Madhusudhan et al.
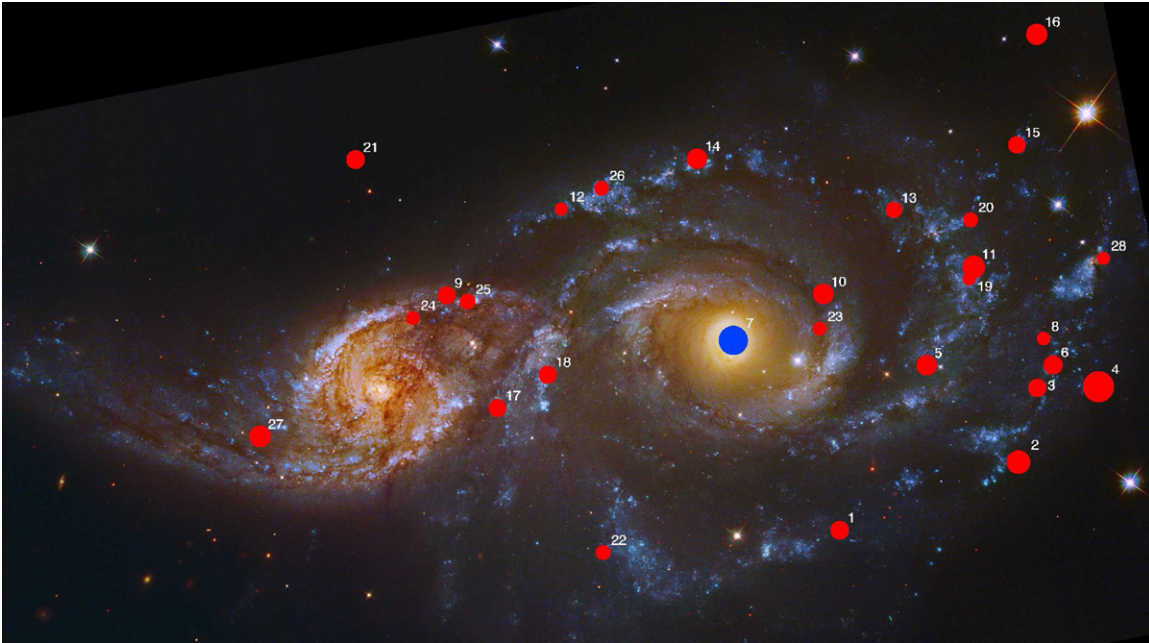
Figure 3. *HST* image of NGC 2207/IC 2163 with the filled red circles superposed indicating the locations of the X-ray point sources detected above the completeness limit. The size of each circle is proportional to the cube root of the luminosity of the individual X-ray source. Each circle is annotated according to the source number in Table 1.

(A color version of this figure is available in the online journal.)

2008), and therefore their numbers and the concomitant position of the break in the XLF may be dependent on the very recent SFR history of the host galaxy.

We predicted the contribution of background AGNs within the $D25$ ellipse above the completeness luminosity based on the work of Georgakakis et al. (2008). Their $\log N - \log S$ function for the 0.5–10 keV band was converted to apply in the broad band of 0.5–8 keV. The result is that ~ 1.7 background AGNs with $L_X > L_{comp}$ are expected to be present and to have a combined luminosity $L_{AGN}(>L_{comp}) = 7.32 \times 10^{39}$ erg s^{-1}. In this work AGN "luminosities" are computed as $4\pi \, D^2 \, S_{AGN}(>S_{comp})$, where D is the distance to the galaxy pair and S_{AGN} is the predicted total flux of background AGNs above the completeness threshold flux S_{comp}. The cumulative luminosity distribution of background AGNs is marked in Figure 4 by a dot-dashed (red) curve. Thus, perhaps one or two of the twenty-two detected sources may actually be background AGNs. In order to plot the background AGN contribution to the luminosity function we convert their flux to "luminosity" as defined as above. Obviously, although this quantity has units of erg s^{-1}, it has nothing to do with the true luminosities of background objects. However, the introduction of this quantity simplifies the calculation of contributions of background objects to the numbers of sources and their total luminosity.

4. STAR FORMATION RATE

The SFR is one of the most important parameters in the investigation of gas-rich galaxies. Over the last decade, several studies have demonstrated the existence of a tight correlation between the *collective* number of luminous X-ray sources and the integrated SFR of late-type host galaxies (e.g., Grimm et al. 2003; Mapelli et al. 2010; Swartz et al. 2011; Mineo et al. 2012). This relation can now be explored in greater detail using spatially resolved images of SFR surface density. Such SFR
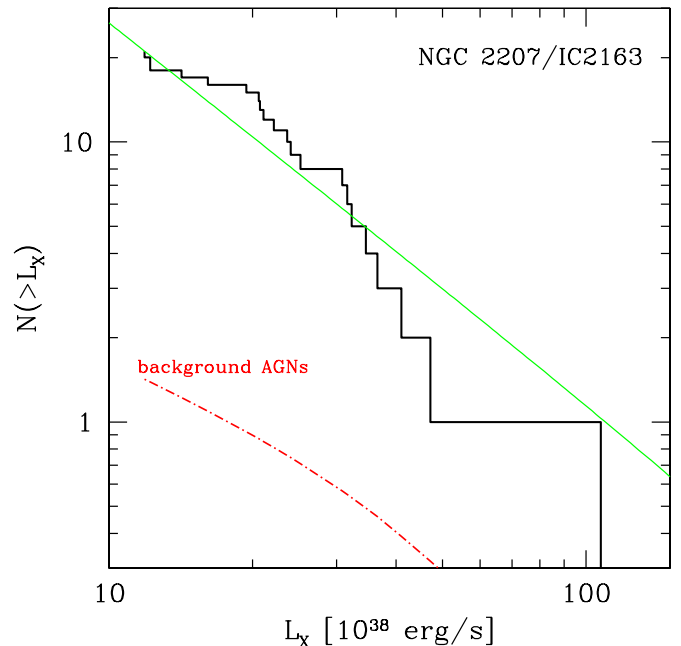

Figure 4. Cumulative X-ray luminosity distribution of the compact sources detected within the $D25$ ellipse, above the completeness luminosity of the galaxy pair NGC 2207/IC 2163 (solid, black line). The central AGN is not included. The dash-dotted (red) curve shows the predicted level of resolved background AGNs, based on results from Georgakakis et al. (2008). The green solid line is the best fitting power law model.

(A color version of this figure is available in the online journal.)

images can be constructed from *Spitzer* and *GALEX* archival data, following a recent technique introduced by Leroy et al. (2008). This will allow us to investigate the spatial distribution of the X-ray point sources and their luminosities as a function of the *local* SFR at their location.
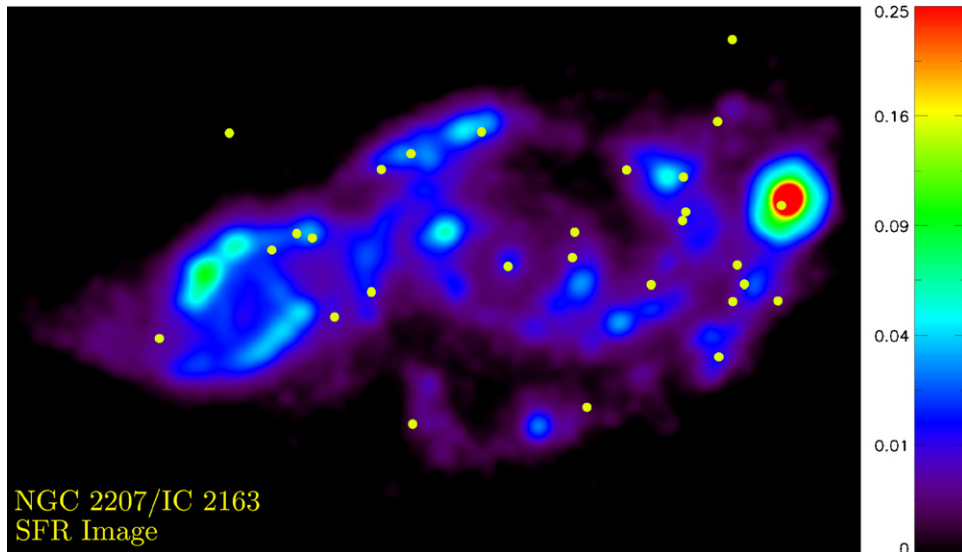
Figure 5. SFR density map for NGC 2207/IC 2163, in units of $M_\odot$ yr^{-1} kpc^{-2}, obtained by combining *GALEX* FUV and *Spitzer* 24 μm images according to the prescription of Leroy et al. (2008). The small yellow circles mark the locations of the X-ray sources. See Section 4.1 for details.

(A color version of this figure is available in the online journal.)

4.1. Star Formation Rate Surface Density Images

We adopted the recipe provided by Leroy et al. (2008) to estimate the spatially resolved SFR distribution in the NGC 2207/IC 2163 system. The SFR density in units of $M_\odot$ yr^{-1} kpc^{-2} was therefore estimated using their Equation (D11):

$$\Sigma_{\rm SFR} = 8.1 \times 10^{-2} I_{\rm FUV} + 3.2 \times 10^{-3} I_{24\,\mu m}, \qquad (5)$$

where $I_{\rm FUV}$ and $I_{24\,\mu m}$ are in units of MJy ster^{-1}. The combination of *GALEX* FUV and *Spitzer* MIPS 24 μm images is relatively easy to implement because of their reasonably similar angular resolutions (4″ and 6″ FWHM, respectively) and sensitivities. The *Spitzer* 24 μm images are already calibrated in MJy ster^{-1}. To convert the *GALEX* FUV images from count rate (count s^{-1}) to MJy ster^{-1} we used the conversion factor $C_{\rm FUV} = 2.028$. This results from converting counts s^{-1} to flux (erg cm^{-2} s^{-1} Å^{-1}),[10] using a factor of 1.40×10^{-15}, and a successive conversion from erg cm^{-2} s^{-1} Å^{-1} to MJy ster^{-1}, involving a factor of 1.45×10^{15}.

Importantly, this SFR estimator is sensitive to both dust-obscured and exposed star formation activity. As the far-ultraviolet (FUV) emission originates from the photospheres of O and B stars, *GALEX* intensities tend to indicate the somewhat older regions of star formation ($\tau_{\rm FUV} \gtrsim 30$ Myr), where the obscuring dust has already been cleared. The 24 μm emission originates from dust grains heated by embedded young ionizing stars and traces the star formation over timescales, $\tau_{24\,\mu m} \sim 5$–10 Myr (Calzetti et al. 2007; S. Rappaport et al. 2012, in preparation; M. Krumholz 2012, private communication). The SFR over these shorter timescales may be more closely related to the upper end of the ULX luminosities (see Section 6).

For the first term of Equation (5) we used publicly available *GALEX* FUV (1529 Å) background-subtracted images from the All Sky Surveys (AIS) program.[11] These images are calibrated

in units of counts per pixel per second, and are also corrected for the relative instrumental response. The units of the FUV image were converted into MJy ster^{-1} prior to combining the latter with the 24 μm image.

The second term in Equation (5) was based on a *Spitzer* MIPS 24 μm large field image. We used the "post Basic Calibrated Data" products which are calibrated in MJy ster^{-1} and suitable for photometric measurements.[12] We measured the 24 μm background in a region away from the galaxy, and subtracted it from the image before combining the latter with the FUV map. As the pixel scales of the 24 μm and FUV images are different (2″.45 pixel^{-1} and 1″.5 pixel^{-1}, respectively), we spatially interpolated the 24 μm image in order to match the better resolution of the *GALEX* FUV image. This was done using the routine HASTROM, from the NASA IDL Astronomy User's Library.[13] The routine properly interpolates without adding significant spatial information (i.e., no spatial frequency content beyond the intrinsic resolution of the original image). In essence, the 24 μm image was simply oversampled. The resulting SFR surface density map is displayed in Figure 5 at the same spatial resolution and with the same pixel coordinates as the *GALEX* FUV image (but limited by the *Spitzer* resolution).

Interestingly, the SFR map shows a similar morphology to the radio emission map at 4.86 GHz, dominated by nonthermal (synchrotron) radiation, discussed by Drzazga et al. (2011; see their Figures 1 and 2).

4.2. Integrated Star Formation Rate

We calculated the overall SFR of the galaxy pair NGC 2207/IC 2163 by integrating Equation (5) inside the $D25$ region. The resulting equation corresponds to the fiducial method from Leroy et al. (2008), in particular to their Equation (D10), on which their prescription for obtaining SFR surface density maps (their Equation (D11)), is based.

The FUV and 24 μm terms for the integrated SFR were obtained by Leroy et al. (2008) assuming a stellar initial mass

---

[10] http://galexgi.gsfc.nasa.gov/docs/galex/FAQ/counts_background.html
[11] http://galex.stsci.edu/GR4/?page=mastform

[12] http://irsa.ipac.caltech.edu/applications/Spitzer/Spitzer/
[13] http://idlastro.gsfc.nasa.gov/

function (IMF) as in Calzetti et al. (2007) (i.e., slope -1.3 for the 0.1–0.5 $M_\odot$ mass range and -2.3 for 0.5–120 $M_\odot$). Using this prescription, we obtained a total SFR of 11.8 $M_\odot$ yr^{-1} integrated within the $D25$ region of the galaxy pair (for the Calzetti et al. 2007 IMF). The corresponding value of SFR based on a Salpeter IMF from 0.1 to 100 $M_\odot$, would be 18.8 $M_\odot$ yr^{-1} (the IMF conversion yields a factor of 1.59 difference). For comparison, the integrated SFRs of the star-forming galaxies NGC 4194, NGC 7541, and the Cartwheel (see, e.g., Wolter & Trinchieri 2004; Crivellari et al. 2009), assuming a Salpeter IMF as above, are 16.8 $M_\odot$ yr^{-1}, 14.7 $M_\odot$ yr^{-1} and 17.6 $M_\odot$ yr^{-1}, respectively (Mineo et al. 2012).

5. SPATIALLY RESOLVED N_X–SFR, L_X–SFR RELATIONS

We investigated the occurrence of the X-ray point sources and their luminosities as a function of the *local* SFR. We started from the SFR density image obtained as described in Section 4.1. A set of SFR density bins with constant logarithmic spacing was defined. The source number and their collective luminosity above L_{comp} (respectively $N_X(L > L_{comp})$ and $L_X(>L_{comp})$) were assigned to each bin of SFR density according to the SFR density value at the position of the source. We counted the number of pixels in each bin of SFR density and their cumulative area. Knowing the area, and based on the $\log N - \log S$ function from Georgakakis et al. (2008), we calculated the predicted number of background AGNs, $N_{AGN}(L > L_{comp})$, and their luminosity, $L_{AGN}(>L_{comp})$, above the completeness luminosity threshold, in accordance with the procedure used in Section 3.2. Typically, this amounts to less than one background source per bin. These two quantities were subtracted to yield $N_X(L > L_{comp})$ and $L_X(>L_{comp})$ respectively and the resulting value was divided by the total area in kpc^2 in each SFR density bin.

The final values of surface density of X-ray point sources (sources kpc^{-2}) and luminosity (erg s^{-1} kpc^{-2}) corrected for background AGNs, are plotted against the value of the SFR surface density in Figure 6. Pixels with SFR density less than 6×10^{-4} $M_\odot$ yr^{-1} kpc^{-2} were not used as they are dominated by background noise. The latter was measured in two large regions of the SFR density image outside the $D25$ ellipse. The resulting mean values in the two regions are $(6.4 \pm 1.3) \times 10^{-5}$ and $(7.3 \pm 0.9) \times 10^{-5}$ $M_\odot$ yr^{-1} kpc^{-2} with rms in the range of 6.4–6.8×10^{-4}.

For comparison with the present measurements, in Figure 6 we also plot the multiple-galaxy-wide average N_X–SFR and L_X–SFR relations for HMXBs obtained in Mineo et al. (2012, their Equations (20) and (22)). Here $N_X = N(L_X \gtrsim 10^{39}$ erg s$^{-1})$ as for the observed data. Since the SFR in the Mineo et al. (2012) relation is based on the Salpeter IMF from 0.1 to 100 $M_\odot$, we first adjusted it to be consistent with the IMF assumed in the Leroy et al. (2008) algorithm (see Section 4.2 for details). We also compare our results with the N_{ULX}–SFR relation from Mapelli et al. (2010), whose definition of N_{ULX} is equal to our N_X. The dashed line in the top panel of Figure 6 shows their Equation (6), which is slightly non-linear.

Figure 6 shows that the global relation between cumulative number of X-ray point sources and the integrated SFR of the host galaxy also holds on *local* scales (top panel). The small-number statistics involved did not allow us to study in any detail the L_X–SFR relation (bottom panel). A more extensive work by S. Mineo et al. (in preparation), based on a significantly larger number of X-ray sources detected in a sample of nearby grand-
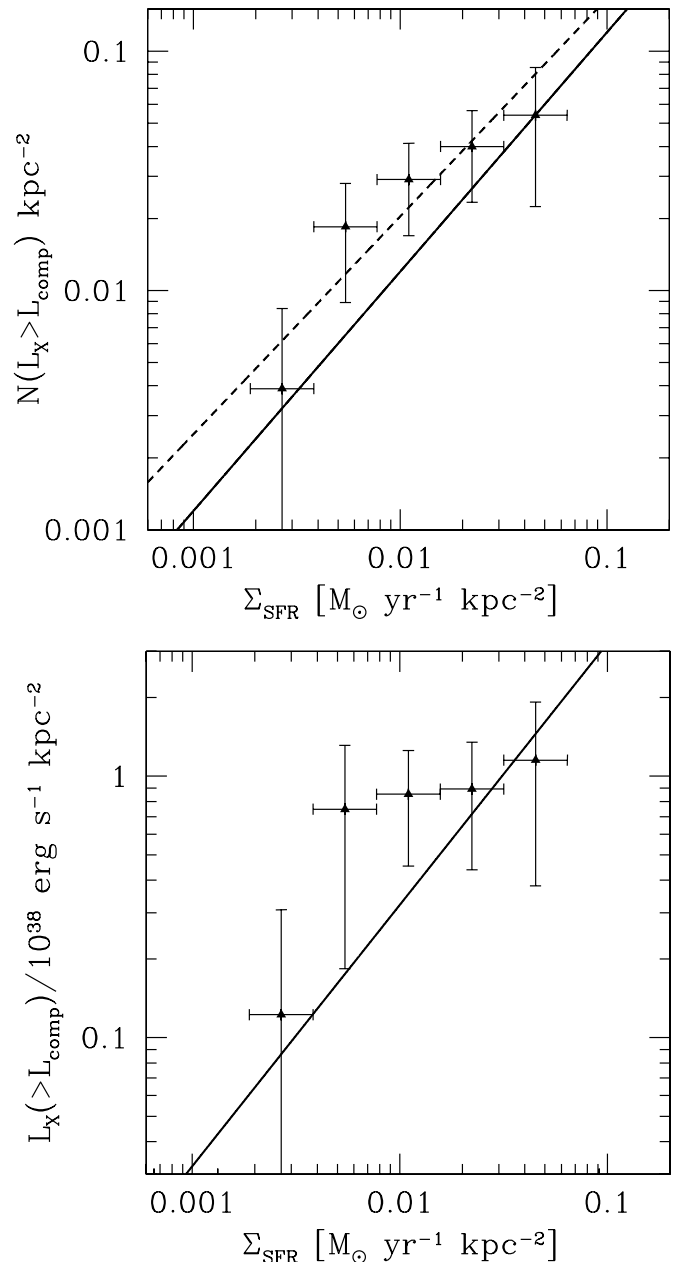

Figure 6. Relation between the *local* SFR density in NGC 2207/IC 2163 ($M_\odot$ yr^{-1} kpc^{-2}) and the number density (N_X/kpc^2, top panel) and luminosity density (L_X/kpc^2, bottom panel) of luminous X-ray sources above our completeness threshold in L_X. Both these quantities are corrected for the contribution of background AGNs. The star formation rate density was computed from the Leroy et al. (2008) algorithm as described in Section 4.1. The solid curves are the galaxy-wide average N_X–SFR (top panel) and L_X–SFR (bottom panel) relations for HMXBs obtained in Mineo et al. (2012, their Equations (20) and (22) respectively). We show them for comparison, rescaled in order to match the IMF assumption in the SFR recipe from Leroy et al. (2008). For these expressions, N_X and L_X are N, $L(L_X \gtrsim 10^{39}$ erg s$^{-1})$, as is the case for the observational data. The dashed line in the top panel is the relation between the galaxy-wide average numbers of ULXs and SFR by Mapelli et al. (2010, their Equation (6)), which is slightly non-linear.

design spiral galaxies, may yield more useful information on the linearity of the latter relation.

6. SFR DENSITY DISTRIBUTION AROUND ULXs

We studied the distribution of the SFR densities around the detected ULXs, with the ultimate aim of constraining the

ULX evolution in relation to the star formation time scale. The analysis that we discuss below is based on the SFR density image shown in Figure 5.

HMXBs can have large runaway velocities due to kicks caused by asymmetric explosions in the formation of the compact object. Since it has been suggested that ULXs might be bright HMXBs (Grimm et al. 2003; Mineo et al. 2012), high spatial velocities may also be relevant to ULXs. A compact object with a high-mass companion can have an average runaway speed of the order of $\sim 40\,\mathrm{km\,s^{-1}}$, in the case of OB supergiant X-ray binaries or $\sim 15\,\mathrm{km\,s^{-1}}$ for Be/X-ray binaries (Chevalier & Ilovaisky 1998). Coe (2005) measured a maximum average speed of $\sim 30\,\mathrm{km\,s^{-1}}$ based on the separation of star clusters and HMXBs in the Small Magellanic Cloud (SMC). Other studies found that the limiting average speed is $\sim 50\,\mathrm{km\,s^{-1}}$ (e.g., van den Heuvel et al. 2000; Kaaret et al. 2004). The average speed among those noted here, $\sim 35\,\mathrm{km\,s^{-1}}$, was adopted as a typical runaway velocity of our luminous X-ray sources. Assuming that the latter move at this speed over a $\sim 30\,\mathrm{Myr}$ lifetime, appropriate for HMXBs and ULXs, they would be displaced by $\sim 1\,\mathrm{kpc}$ at the end of their lives with respect to their location at birth. At the distance of NGC 2207/ IC 2163 this corresponds to a maximum proper motion of $\sim 5\farcs5$. The latter value was therefore used as the radius of each of the fiducial circular regions immediately surrounding the 21 high-luminosity X-ray sources in which to measure the level of local SFR activity.

We divided the sources into three groups according to their X-ray luminosities: $L_{\mathrm{comp}} < L_X \leqslant 2 \times 10^{39}\,\mathrm{erg\,s^{-1}}$, $2 \times 10^{39}\,\mathrm{erg\,s^{-1}} < L_X \leqslant 3 \times 10^{39}\,\mathrm{erg\,s^{-1}}$, and $L_X > 3 \times 10^{39}\,\mathrm{erg\,s^{-1}}$. The three groups include six, seven and eight sources, respectively. For each group, we created a corresponding SFR density image by selecting, from the original SFR density map, only the pixels which are covered by the fiducial circular regions centered on the sources in that luminosity group. In addition, we created an SFR density map for the area of the $D25$ ellipse where no sources were detected, by excluding the fiducial circular regions of all detected sources. Histograms of the values in these four images show the distributions of SFRs in the vicinities of the sources in each group and, to act as a control, in the regions away from all sources (see Figure 7).

The peaks of the histograms for the three ULX groups appear to shift slightly (by at most a factor of ~ 2) toward *higher* SFR densities values as the X-ray luminosity range *decreases*. This is opposite to what one might have naively guessed. The slight trend is driven by the $24\,\mu\mathrm{m}$ emission rather than the FUV emission, i.e., by the younger ($\lesssim 10\,\mathrm{Myr}$, Calzetti et al. 2007; S. Rappaport et al. 2012, in preparation) star formation tracer of the two ingredients used to construct the SFR density image. A vertical dashed line corresponding to the position of the peak in the histogram for the brightest sources is plotted in Figure 7. More in line with expectations, the distribution for the regions away from the sources peaks at much lower SFR densities. This shows that the fraction of pixels having high SFR density, ~ 0.01–$0.03\,M_\odot\,\mathrm{yr^{-1}\,kpc^{-2}}$, is much higher in the vicinity of bright X-ray sources, than in the field as a whole. This confirms our expectation that ULXs tend to be located close to star-forming regions.

To quantify the consistency, or lack thereof, among the three distributions (top three panels in Figure 7), we performed a KS test. The three KS D values are $D_{H,M} = 0.18$, $D_{H,L} = 0.24$ and $D_{M,L} = 0.13$, respectively between the histograms for high and middle, high and low, and middle and low luminosity
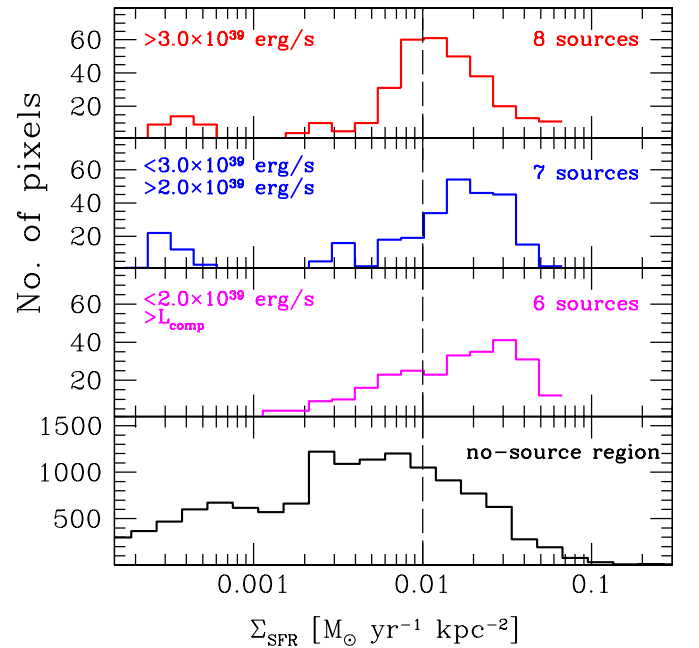

Figure 7. Distribution of SFR density values surrounding the ULXs in NGC 2207/IC 2163. The SFR density was computed as described in Section 6 in the regions immediately surrounding the 21 individual X-ray sources in the colliding galaxy pair. From top to bottom, the histograms show the distribution of SFR density values around X-ray sources more luminous than $3 \times 10^{39}\,\mathrm{erg\,s^{-1}}$ (red), around sources with $2 \times 10^{39}\,\mathrm{erg\,s^{-1}} < L_X \leqslant 3 \times 10^{39}\,\mathrm{erg\,s^{-1}}$ (blue), around sources with $L_{\mathrm{comp}} < L_X \leqslant 2 \times 10^{39}\,\mathrm{erg\,s^{-1}}$ (magenta) and for all pixels where no sources were detected (black). To generate all four histograms we considered only points inside of the $D25$ contour of the galaxy pair. The histogram peaks for the three ULX groups are shifted slightly toward higher SFRs as the X-ray luminosity range decreases. The trend is driven by the FIR emission. In a more compelling way, the regions with no source detections peak at much lower values of SFR densities than where the X-ray sources are found.

(A color version of this figure is available in the online journal.)

groups shown in Figure 7. This yields two-sided KS statistics probabilities of $\sim 3.1 \times 10^{-5}$, $\sim 6.5 \times 10^{-8}$, and $\sim 1.7 \times 10^{-2}$ respectively, indicating that the histograms are likely drawn from different underlying distributions. Note that the KS test tends to emphasize the region near the peak of the distribution, i.e., the region where the best Poisson statistics is obtained. Additionally, both systematic errors in estimating the SFR rate, as well as correlations in SFR among neighboring pixels, make the error estimates for these histograms difficult to evaluate. With these caveats, and using the present data, we conclude that the ULX luminosity does not seem to depend strongly on the local SFR around the source, but further studies with larger samples will help clarify the situation. There is little doubt, however, that there is a significant difference between the SFRs near ULXs and those from source-free regions.

Figure 7 also reinforces the conclusion found with regard to the N_X–SFR and L_X–SFR relations, shown in Figure 6, that while the *numbers* of ULXs are significantly correlated with the local SFR densities, the *luminosities* of those sources do not appear to be so correlated.

7. TOTAL X-RAY LUMINOSITY PER UNIT SFR

After having subtracted the predicted contribution from background AGNs, the collective X-ray luminosity of the compact source population with $L_X > L_{\mathrm{comp}}$ within the $D25$ ellipse is $L_{\mathrm{XRB}}(0.5\text{–}8\,\mathrm{keV}) = (5.33 \pm 0.37) \times 10^{40}\,\mathrm{erg\,s^{-1}}$. The

total SFR integrated within the same region (Section 4.2) is 11.8 $M_\odot$ yr^{-1}.

We compare this result with the more extensive results of Mineo et al. (2012). First, we estimate the integrated SFR of NGC 2207/IC 2163 following the same method used in the latter paper, and that is based on the recipe of Iglesias-Páramo et al. (2006), which assumes a Salpeter IMF from 0.1 to 100 $M_\odot$: SFR = SFR$^0_{\rm NUV}$ + SFR$_{\rm IR}$. NUV^0 is the near-ultraviolet (2312 Å) luminosity uncorrected for dust attenuation and IR is the 8–1000 μm luminosity (see Section 5 of Mineo et al. 2012, for details). We obtain a total SFR of 23.7 $M_\odot$ yr^{-1}, similar to that obtained in Section 4.2 under the same IMF assumption (cf. 18.8 $M_\odot$ yr^{-1}; SFR estimations usually have uncertainties of ∼50%). In general, FUV and NUV emissions are consistent with each other within 5%–7%, so the main difference between the relation above and the integrated SFR measured as described in Section 4.2, is due to the different IR estimator.

Using the calibration from Mineo et al. (2012, their Equation (22)), we find that the above SFR implies that $L_{\rm XRB}(>10^{36}$ erg s$^{-1}) = 23.7 \times 2.6 \times 10^{39} = 6.2 \times 10^{40}$ erg s^{-1}. Taking into account the difference in the luminosity limit, by integrating the HMXB luminosity distribution from the same paper, we obtain $L_{\rm XRB}(>L_{\rm comp}) = 4.8 \times 10^{40}$ erg s^{-1}. The total X-ray luminosity measured for NGC 2207/IC 2163 is in agreement with the latter result to within ∼10%. Analogously, we can use the same SFR, in Equation (20) of Mineo et al. (2012), to predict that $N_{\rm XRB}(L > L_{\rm comp}) = 17.9$, for the same luminosity threshold. Comparing this with the observed number of sources, 19.3, the agreement is rather good (the difference between the solid line and the points in Figure 6 is much larger, due to the different method of calculating the SFR). This supports the suggestive results by Grimm et al. (2003) that the ULX population—at least at the bottom end of their luminosity range—might be an extension of the HMXB population at high luminosities.

8. DISCUSSION

In Figures 1, 3, and 5 it appears that IC 2163 is forming stars more actively than NGC 2207 (note the much more extensive dust and gas content in the former), although the latter galaxy hosts most of the detected ULXs. A comparison between UV and 24 μm emissions (Figure 1) shows that the latter is more enhanced, suggesting that the star formation activity in IC 2163 may be more recent (<10 Myr). This might indicate a possible age effect in the distribution of ULXs (see, e.g., Sections 7.2 and 7.3 in Shtykovskiy & Gilfanov 2005). The specific SFR, i.e., the SFR per unit stellar mass, could help us in investigating the latter hypothesis. We measured the integrated SFR and stellar mass of the two galaxies separately. The area of the sky covered by IC 2163 was defined by visually inspecting its optical and infrared images. We did not use the $D25$ ellipse as it includes a large fraction of the nearby NGC 2207. The SFR was estimated as described in Section 7 and the stellar mass using the K_S-band image from the 2MASS Large Galaxy Atlas (LGA),[14] assuming an effective $B-V$ color of 0.67 mag (provided by HyperLeda[15]) and using the calibration from Bell & de Jong (2001).

The integrated SFR of IC 2163 is 9.1 $M_\odot$ yr^{-1} and its inferred stellar mass is 5.2×10^{10} $M_\odot$. Five ULXs out of twenty-one are located within its area. This yields a $N_{\rm X}$/SFR $\simeq 0.55 \pm 0.25$ $(M_\odot$ yr$^{-1})^{-1}$ and specific star formation rate SFR/M$_\star \simeq$

Table 2
Summary of Star Formation Rates

Galaxy	$L_{\rm X}^{\rm tot}$ (10^{40} erg s^{-1})	M_* (10^{11} $M_\odot$)	SFR ($M_\odot$ yr^{-1})	SFR/M_* (10^{-10} yr^{-1})	$N_{\rm X}$/SFR (yr $M_\odot^{-1}$)
(1)	(2)	(3)	(4)	(5)	(6)
NGC 2207	4.3 ± 0.3	1.2	14.6	1.22	1.09 ± 0.27
IC 2163	1.0 ± 0.2	0.52	9.1	1.75	0.55 ± 0.25
Entire D_{25}	5.3 ± 0.4	1.7	23.7	1.39	0.89
Antennae	1.7	0.31	5.4	1.74	0.93

Notes. Column 1: galaxy; Column 2: collective 0.5–8 keV luminosity of the compact source population with $L_{\rm X} > 10^{39}$ erg s^{-1}; Column 3: mass in stars; Column 4: total star formation rate, SFR $= 4.6 \times 10^{-44} L_{\rm IR} + 1.2 \times 10^{-43} L_{\rm NUV,obs}$ as described in Section 7; Column 5: specific star formation rate; Column 6: number of luminous X-ray sources per unit SFR.

1.75×10^{-10} yr^{-1}. Subtracting these values from those measured within the entire $D25$ ellipse of the galaxy pair, we estimated for NGC 2207 a total SFR of 14.6 $M_\odot$ yr^{-1} and stellar mass 1.2×10^{11} $M_\odot$. This yields a SFR/M$_\star \sim 1.22 \times 10^{-10}$ yr^{-1} and $N_{\rm X}$/SFR $\sim 1.09 \pm 0.27$ $(M_\odot$ yr$^{-1})^{-1}$. The difference in specific SFR is not large. The difference in $N_{\rm X}$/SFR is only marginally significant. The source number in IC 2163 is a factor of 1.4 lower than that predicted by the calibration from Mineo et al. (2012), while in the rest of the merging system it is a factor of 1.5 higher than predicted.

We can compare these properties with those of the Antennae (NGC 4038/39). Using the same method as above to estimate the integrated SFR and stellar mass, Mineo et al. (2012) obtain SFR $= 5.4$ $M_\odot$ yr^{-1} and $M_\star = 3.1 \times 10^{10}$ $M_\odot$. Within the same area of sky the same authors detected five ULXs. This corresponds to only somewhat larger numbers of ULXs per unit mass and per unit SFR in comparison with those of NGC 2207/IC 2163.

The above results for galaxy masses, SFRs, specific SFRs, and luminous X-ray sources per SFR are summarized in Table 2.

We tried to identify possible counterparts to the 21 ULXs hosted by NGC 2207/IC 2163. We cross-matched their locations with the Naval Observatory Merged Astrometric Dataset (NOMAD;[16] Zacharias et al. 2004). This catalog is a merger of data from the *Hipparcos*, *Tycho-2*, UCAC-2, and USNO-B1 catalogs, supplemented by photometric information from the 2MASS final release point source catalog. We used a match radius of 2″, keeping in mind that the 99% uncertainty circle of *Chandra* absolute positions for sources within 3′ of the aimpoint is 0″.8. The choice of a 2″ match radius is rather conservative considering that the typical mean error on coordinates in the NOMAD catalog is also ≲0″.8. We found possible counterparts in the USNO B1.0 catalog for seven ULXs, i.e., source Nos. 2, 4, 7, 14, 15, 25, and 28. For all these objects, the catalog provides, among other measurements, the *B*- and *R*-band magnitudes and the proper motions. All the optical objects are separated from the corresponding *Chandra* ULX positions by angular distances ranging from 1″.2 (for source 14) to 2″.0 (for source No. 4). Based on the accuracy of the absolute Chandra positions, this indicates that there are no compelling candidate counterparts among the nearly matched sources. Moreover, sources 2, 4 and 15 have measured proper motions, which indicate that these are most probably foreground objects. A more accurate search of the ULX counterparts would require the use of *HST* data, which are

publicly available in the *HST* archive. A forthcoming paper will include such a study.

The search for optical counterparts can also be useful to identify possible background AGNs among our ULX sample. In particular, sources 4, 16, 21 and 27 are located outside the spiral structures of the two galaxies. For the latter three there is no counterpart in NOMAD. As mentioned above, one match was found for source 4, with a separation of $\approx 2''.0$ from its *Chandra* coordinates. This source is the brightest X-ray object detected in the vicinity of NGC 2207/IC 2163. The *R*-band magnitude of the optical object is 14.7. This can be converted into a flux $f_R \simeq 1.7 \times 10^{-11}$ erg cm^{-2} s^{-1} which yields, in turn, $\log(f_{0.5-8\,\mathrm{keV}}/f_R) \simeq -2.4$. According to Bauer et al. (2004) this object should then not be an AGN. This is further supported by the fact that the hardness ratio of source 4 differs from that of the central AGN in NGC 2207 (see Table 1). However, we note that low luminosity AGNs populate the same region of the X-ray flux versus *R*-band magnitude plane (Figure 7 in Bauer et al. 2004) as our source 4. On statistical grounds, the predicted number of background sources above the luminosity of source 4 is only 0.09. For a Poisson distribution, the probability that the brightest ULX in our galaxy pair is a background AGN is only 8%. Assuming that the observed XLF of the ULXs extends to the highest luminosities with the same slope, the predicted number of X-ray sources above the same threshold would be 1. Thus, a ULX interpretation for source 4 is the most likely.

9. SUMMARY AND CONCLUSIONS

We have introduced a new technique to investigate the spatial and luminosity distributions of X-ray binaries in star forming galaxies as a function of the *local* SFRs. We have applied this technique to study the population of 21 ULXs in the colliding galaxy pair NGC 2207/IC 2163. This is comparable with the largest number of ULXs per unit mass in any galaxy that we know of, in particular, the Antennae.

Using the prescription by Leroy et al. (2008), we constructed an image of SFR density, in units of $M_\odot$ yr^{-1} kpc^{-2}, of NGC 2207/IC 2163, by combining the *GALEX* FUV and *Spitzer* 24 μm images. We find that the global relation between the cumulative number of X-ray point sources and the integrated SFR of the host galaxy also holds on *local* scales. We were not able to investigate in detail the corresponding local L_X–SFR relation due to the small number of X-ray sources.

We studied the distribution of the SFR density around the detected ULXs, with the ultimate aim of constraining the ULX evolution in relation to the star formation time scale. We find that the peaks in the SFR density distributions around ULXs appear to shift slightly toward *higher* SFR density values as the X-ray luminosity range *decreases*. The regions with no source detections, however, do peak at much lower SFR densities than where the X-ray sources are found. The fraction of pixels having high SFR density, ~ 0.01–0.03 $M_\odot$ yr^{-1} kpc^{-2}, is higher in the vicinity of bright X-ray sources, than in the field.

We find that the number and luminosity of ULXs per unit SFR are in agreement, to within 10%, with those predicted by the global relations of Mineo et al. (2012). This supports the suggestion of Grimm et al. (2003) that the lower luminosity end of the ULX population (e.g., 1–3×10^{39} erg s^{-1}) might be an extension of the HMXB population to higher luminosities.

We attempted to investigate possible age effects in the distribution of ULXs across the galaxy pair NGC 2207/IC 2163. We find that the difference in specific SFR (SFR/M$_\star$) between

NGC 2207 and IC 2163 is not large. The difference in N_X/SFR is only marginally significant. The source number in IC 2163 is a factor of 1.4 lower than that predicted by the calibration from Mineo et al. (2012), while in the rest of the merging system it is a factor of 1.5 higher than predicted.

We tried to identify possible counterparts to the 21 ULXs hosted by NGC 2207/IC 2163. In particular, our search of the USNO-B1 catalog emphasized possible optical counterparts to the brightest detected source (No. 4), as well as for sources 16, 21, and 27, which are located *outside* the spiral structures of the two galaxies. In general, the relatively large separations (i.e., $\gtrsim 1''$) between possibly interesting stellar images and the *Chandra* coordinates suggest that there are no compelling candidate counterparts. The closest optical object to the brightest detected source (No. 4) found in the USNO-B1 catalog does not have the properties of a background AGN. A more definitive search for ULX counterparts would require the use of *HST* data, which is publicly available in the *HST* archive. We plan to pursue this in a forthcoming paper.

Note added to the manuscript. After this work was complete, we learned from M. Kaufman (2013, private communication) of some useful comparisons with their earlier *XMM-Newton* observations of NGC 2207/IC 2163 (Kaufman et al. 2012). In particular, *Chandra* source 11 apparently coincides with a variable, nonthermal radio source, and is therefore more likely to be a background AGN than a ULX. The soft, extended *Chandra* X-ray source 28 is close to the radio core of *feature i* in Kaufman et al. (2012), and the extended emission is likely to come from this starburst region.

REFERENCES

Appleton, P. N., Charmandaris, V., & Struck, C. 1996, ApJ, 468, 532
Arnett, W. D. 1982, ApJ, 254, 1
Bauer, F. E., Alexander, D. M., Brandt, W. N., et al. 2004, AJ, 128, 2048
Belczynski, K., Bulik, T., Fryer, C. L., et al. 2010, ApJ, 714, 1217
Bell, E. F., & de Jong, R. S. 2001, ApJ, 550, 212
Calzetti, D., Kennicutt, R. C., Engelbracht, C. W., et al. 2007, ApJ, 666, 870
Chevalier, C., & Ilovaisky, S. A. 1998, A&A, 330, 201
Coe, M. J. 2005, MNRAS, 358, 1379

Colbert, E. J. M., & Mushotzky, R. F. 1999, ApJ, 519, 89
Crivellari, E., Wolter, A., & Trinchieri, G. 2009, A&A, 501, 445
de Vaucouleurs, G., de Vaucouleurs, A., Corwin, H. G., Jr., et al. 1991, Third Reference Catalogue of Bright Galaxies, Vol. 1-3 (New York: Springer) 2069
Drzazga, R. T., Chyży, K. T., Jurusik, W., & Wiórkiewicz, K. 2011, A&A, 533, A22
Elmegreen, B. G., Kaufman, M., Struck, C., et al. 2000, AJ, 120, 630
Elmegreen, D. M., Elmegreen, B. G., Kaufman, M., et al. 2006, ApJ, 642, 158
Fabbiano, G. 2005, Sci, 307, 533
Farrell, S. A., Webb, N. A., Barret, D., Godet, O., & Rodrigues, J. M. 2009, Natur, 460, 73
Feng, H., & Soria, R. 2011, NewAR, 55, 166
Gao, Y., Wang, Q. D., Appleton, P. N., & Lucas, R. A. 2003, ApJL, 596, L171
Georgakakis, A., Nandra, K., Laird, E. S., Aird, J., & Trichas, M. 2008, MNRAS, 388, 1205
Gerber, R. A., Lamb, S. A., & Balsara, D. S. 1992, ApJL, 399, L51
Grimm, H.-J., Gilfanov, M., & Sunyaev, R. 2003, MNRAS, 339, 793
Higdon, J. L. 1995, ApJ, 455, 524
Higdon, J. L., & Wallin, J. F. 1997, ApJ, 474, 686
Iglesias-Páramo, J., Buat, V., Takeuchi, T. T., et al. 2006, ApJS, 164, 38
Kaaret, P., Alonso-Herrero, A., Gallagher, J. S., et al. 2004, MNRAS, 348, L28
Kalberla, P. M. W., Burton, W. B., Hartmann, D., et al. 2005, A&A, 440, 775
Kaufman, M., Grupe, D., Elmegreen, B. G., et al. 2012, AJ, 144, 156
Kennicutt, R. C., Jr. 1998, ARA&A, 36, 189
King, A. R. 2004, MNRAS, 347, L18
Leroy, A. K., Walter, F., Brinks, E., et al. 2008, AJ, 136, 2782
Lynds, R., & Toomre, A. 1976, ApJ, 209, 382

Madhusudhan, N., Rappaport, S., Podsiadlowski, P., & Nelson, L. 2008, ApJ, 688, 1235
Mapelli, M., Ripamonti, E., Zampieri, L., Colpi, M., & Bressan, A. 2010, MNRAS, 408, 234
Mihos, J. C., & Hernquist, L. 1994, ApJL, 431, L9
Mineo, S., Gilfanov, M., & Sunyaev, R. 2012, MNRAS, 419, 2095
Özel, F., Psaltis, D., Narayan, R., & McClintock, J. E. 2010, ApJ, 725, 1918
Portegies Zwart, S. F., Baumgardt, H., Hut, P., Makino, J., & McMillan, S. L. W. 2004, Natur, 428, 724
Rappaport, S., Levine, A., Pooley, D., & Steinhorn, B. 2010, ApJ, 721, 1348
Shtykovskiy, P., & Gilfanov, M. 2005, A&A, 431, 597
Smith, B. J., Swartz, D. A., Miller, O., et al. 2012, AJ, 143, 144
Struck, C., Kaufman, M., Brinks, E., et al. 2005, MNRAS, 364, 69
Swartz, D. A., Ghosh, K. K., Tennant, A. F., & Wu, K. 2004, ApJS, 154, 519
Swartz, D. A., Soria, R., Tennant, A. F., & Yukita, M. 2011, ApJ, 741, 49
Swartz, D. A., Tennant, A. F., & Soria, R. 2009, ApJ, 703, 159
Toomre, A. 1978, Large Scale Structures in the Universe (Dordrecht: Reidel) 109
van den Heuvel, E. P. J., Portegies Zwart, S. F., Bhattacharya, D., & Kaper, L. 2000, A&A, 364, 563
Volonteri, M. 2010, Natur, 466, 1049
Voss, R., & Gilfanov, M. 2006, A&A, 447, 71
Voss, R., & Gilfanov, M. 2007, A&A, 468, 49
Whitmore, B. C., & Schweizer, F. 1995, AJ, 109, 960
Wolter, A., & Trinchieri, G. 2004, A&A, 426, 787
Wolter, A., Trinchieri, G., & Colpi, M. 2006, MNRAS, 373, 1627
Yukita, M., Swartz, D. A., Tennant, A. F., & Soria, R. 2010, AJ, 139, 1066
Zacharias, N., Monet, D. G., Levine, S. E., et al. 2004, BAAS, 36, 1418
Zezas, A., & Fabbiano, G. 2002, ApJ, 577, 726